*Stanford Exploration Project, Report 120, May 3, 2005, pages 77–104*

# Angle-domain common image gathers for anisotropic migration

*Biondo Biondi*[1]

**ABSTRACT**

I present a general methodology for computing and analyzing Angle Domain Common Image Gathers (ADCIGs) in conjunction with anisotropic wavefield-continuation migration. I demonstrate that the aperture angles estimated by transforming prestack images using slant stacks along the subsurface-offset axis are a good approximation of the phase aperture angles, and that they are exactly equal to the phase aperture angles for flat events in VTI media.

I introduce a generalization of the concept of migration impulse response for the computation of prestack images function of the subsurface offset that enables a straightforward analytical analysis of the reflector movements caused by perturbations in anisotropic parameters. This analysis shows that the Residual Moveout (RMO) in migrated ADCIGs is function of both the phase aperture angle and the group aperture angle. The dependency of the RMO function on the group angles adds some complexity to the RMO analysis because the computation of group angles from phase angles, which are measured from the ADCIGs, depends on the local background anisotropic velocity at the reflector point.

Several numerical examples demonstrate the accuracy of the RMO function predicted by my kinematic analysis, and in contrast, that the approximation of the group angles by the phase angles may lead to substantial errors for events reflected at wide aperture angles.

## INTRODUCTION

Angle Domain Common Image Gathers (ADCIGs) are a useful tool for updating migration velocity after wavefield-continuation migration (Biondi and Sava, 1999; Clapp and Biondi, 2000). When the migration velocity is not accurate, the inconsistency of the migrated events along the aperture-angle axis is proportional to the migration velocity errors and provides the quantitative information necessary to update the velocity function.

All the methods for computing ADCIGs currently available in the literature are limited to isotropic migration; this is true for both the methods applied during downward continuation before imaging (Prucha et al., 1999), and the methods applied on the prestack migrated image as a post-processing operator (Sava and Fomel, 2003; Rickett and Sava, 2002; Biondi and Tisserant, 2004). Similarly, the quantitative analysis of the residual moveout measured in ADCIGs caused by migration-velocity errors is also limited to the isotropic case (Biondi and Symes, 2003; Biondi and Tisserant, 2004).

[1]**email:** not available

In this paper I generalize the methodologies for computing and analyzing ADCIGs to prestack images obtained by wavefield-continuation anisotropic migration. This work is practically motivated by two current trends in the seismic exploration industry: 1) data are recorded with increasingly long offsets, improving the resolution and reliability of the estimation of anisotropic parameters from surface data, 2) anisotropic prestack depth migration is increasingly being used in areas, like near or under salt bodies, where the image quality, and consequently the velocity estimation process, could benefit from the use of wavefield-continuation migration (Bear et al., 2003; Sarkar and Tsvankin, 2004a). In this perspective, other papers in this report present complementary work that is aimed at developing methods for cost-efficient anisotropic 3-D prestack migration (Sen and Biondi, 2005), and overturned-events anisotropic 3-D prestack migration (Shan and Biondi, 2005b,a).

Sarkar and Tsvankin (2003, 2004b) analyze the effect of velocity errors on offset-domain CIGs produced by Kirchhoff migration. They demonstrate the effectiveness of their method by successfully applying it to a West Africa data set (Sarkar and Tsvankin, 2004a). In this paper, I provide the basic analytical tools necessary to perform anisotropic migration velocity analysis for data sets that benefit from imaging with wavefield-continuation migration instead of Kirchhoff migration.

The main conceptual differences between isotropic ADCIGs and anisotropic ADCIGs are related to the fact that in anisotropic wave-propagation the phase angles and velocities are different from the group angles and velocities (Tsvankin, 2001). Therefore, the first question that I will address is: which aperture angles are we measuring in the ADCIGs? I demonstrate that the transformation to angle domain maps the reflection into the phase-angle domain. Strictly speaking this mapping is exact only for events normal to the isotropic axis of symmetry (e.g. flat events for Vertical Transverse Isotropic (VTI) media), because the presence of dips skews the estimates in ways similar to when geological-dips bias the estimation of aperture angles while computing ADCIGs for converted events (Rosales and Rickett, 2001; Rosales and Biondi, 2005). Fortunately, in the anisotropic case, the biases caused by geological dips are less likely to create problems in practical applications than in the converted waves case. The simple numerical examples shown in this paper seem to indicate that, for realistic values of anisotropy, the errors caused by the geological dips is small and can be neglected. This approximation greatly simplifies the computation of ADCIGs and thus makes their application more attractive.

The second question I address is: is the residual moveout caused by velocity errors only function of the phase angles, or does it also depend on the group angles? In the second part of this paper I demonstrate that the residual moveout is function of both the angles and that neglecting its dependency on the group angles leads to substantial inaccuracy in the predicted RMO function.

## PHASE AND GROUP ANGLES AND VELOCITIES

In anisotropic media the group angles and velocities do not coincide with the phase angles and velocities. The transformation from phase velocity $\widetilde{V}$ to group velocity $V$ is conventionally

defined as the following (Tsvankin, 2001):

$$V = \sqrt{\widetilde{V}^2 + \left(\frac{d\widetilde{V}}{d\widetilde{\theta}}\right)}, \tag{1}$$

where $\widetilde{\theta}$ is the phase propagation angle. The associated transformation from phase angles to group angles $\theta$ is defined as:

$$\tan\theta = \frac{\tan\widetilde{\theta} + \frac{1}{\widetilde{V}}\frac{d\widetilde{V}}{d\widetilde{\theta}}}{1 - \frac{1}{\widetilde{V}}\frac{d\widetilde{V}}{d\widetilde{\theta}}\tan\widetilde{\theta}}. \tag{2}$$

Notice that throughout this paper I use the tilde symbol to distinguish between phase quantities (with a tilde) and group quantities (without a tilde).

Dellinger and Muir (1985) propose, and heuristically motivate, the following symmetric relations for the inverse transforms:

$$\widetilde{S} = \sqrt{S^2 + \left(\frac{dS}{d\theta}\right)}, \tag{3}$$

where $\widetilde{S}$ and $S$ are respectively the phase slowness and the group slowness, and

$$\tan\widetilde{\theta} = \frac{\tan\theta + \frac{1}{S}\frac{dS}{d\theta}}{1 - \frac{1}{S}\frac{dS}{d\theta}\tan\theta}. \tag{4}$$

I use the heuristic relation in equation 4 to derive some of the analytical results presented in this paper. Furthermore, I use all the above relationships to compute the kinematic numerical results presented in this paper.

The numerical results, though not the analytical results, are also dependent on the choice of a specific approximation of the anisotropic phase-velocity function. I used the following VTI approximation for the phase velocity:

$$\widetilde{V}^2_{\rm VTI}(\theta) = \frac{{V_V}^2\cos^2\theta + {V_H}^2\sin^2\theta + \sqrt{\left({V_V}^2\cos^2\theta + {V_H}^2\sin^2\theta\right)^4 + {V_V}^2\left({V_N}^2 - {V_H}^2\right)\sin^2 2\theta}}{2}, \tag{5}$$

where $V_V$, $V_H$, $V_N$, are respectively the vertical velocity, the horizontal velocity and the NMO velocity. Following Fowler (2003), the corresponding approximation for the group velocity is the following:

$$S^2_{\rm VTI}(\theta) = \frac{{S_V}^2\cos^2\theta + {S_H}^2\sin^2\theta + \sqrt{\left({S_V}^2\cos^2\theta + {S_H}^2\sin^2\theta\right)^4 + {S_V}^2\left({S_N}^2 - {S_H}^2\right)\sin^2 2\theta.}}{2}, \tag{6}$$

where $S_V$, $S_H$, $S_N$, are respectively the vertical slowness, the horizontal slowness and the NMO slowness.

The numerical results obtained by modeling and migrating synthetic seismic data were obtained by source-receiver depth continuation (upward for modeling and downward for migration) using the following dispersion relation:

$$k_z = \frac{\omega}{V_V}\sqrt{\frac{\omega^2 - {V_H}^2 k_x^2}{\omega^2 + \left({V_N}^2 - {V_H}^2\right) k_x^2}}, \tag{7}$$

where $\omega$ is the temporal frequency, and $k_x$ and $k_z$ are respectively the horizontal and vertical wavenumbers. The dispersion relation shown in equation 7 corresponds to the velocity and slowness functions in equations 5 and 6 (Fowler, 2003).

### Anisotropic parameters used for numerical tests

To verify the accuracy of the results under realistic but different anisotropic conditions, in the numerical examples I used three set of anisotropic Thomsen parameters representing three different rocks described by Tsvankin (2001):

- Taylor Sand : $\epsilon = 0.110$ $\delta = -0.035$, $\rightarrow \eta = .155$,
- Mesa Clay Shale : $\epsilon = 0.189$, $\delta = 0.204 \rightarrow \eta = -.010$,
- GreenLight River Shale : $\epsilon = 0.0975$, $\delta = -0.11$, $\rightarrow \eta = .266$.

Notice that the GreenLight River Shale is derived from the Green River Shale described by Tsvankin (2001) by halving the anisotropic parameters ($\epsilon$ and $\delta$), because the strong unelliptical nature of the original one ($\eta = .74$) caused the group-slowness approximation in equation 6 to break down, and made the kinematic computations based on ray tracing, and thus on group velocity and angles, inconsistent with wavefield migrations based on the dispersion relation in equation 7. Notice that the GreenLight River Shale is still the most unelliptical among the set of rocks I am using.

## ANGLE GATHERS BY ANISOTROPIC DOWNWARD-CONTINUATION MIGRATION

In anisotropic media, when the reflector is dipping with respect to the normal to the isotropic axis of symmetry (horizontal direction for VTI) the incident and reflected aperture angle differ. This difference is caused by the fact that, although the phase slowness is function of the propagation angle, Snell law requires that the components parallel to the reflector of the incident and reflected slowness vectors must match at the interface. However, we can still define an "average" aperture angle $\widetilde{\gamma}$ and "average" dip angle $\widetilde{\alpha}_x$ using the following relationships:

$$\widetilde{\gamma} = \frac{\widetilde{\beta}_r - \widetilde{\beta}_s}{2}, \quad \text{and} \quad \widetilde{\alpha}_x = \frac{\widetilde{\beta}_s + \widetilde{\beta}_r}{2}, \tag{8}$$

where the $\widetilde{\beta}_s$ and $\widetilde{\beta}_r$ are the phase angles of the downgoing and upgoing plane waves, respectively.

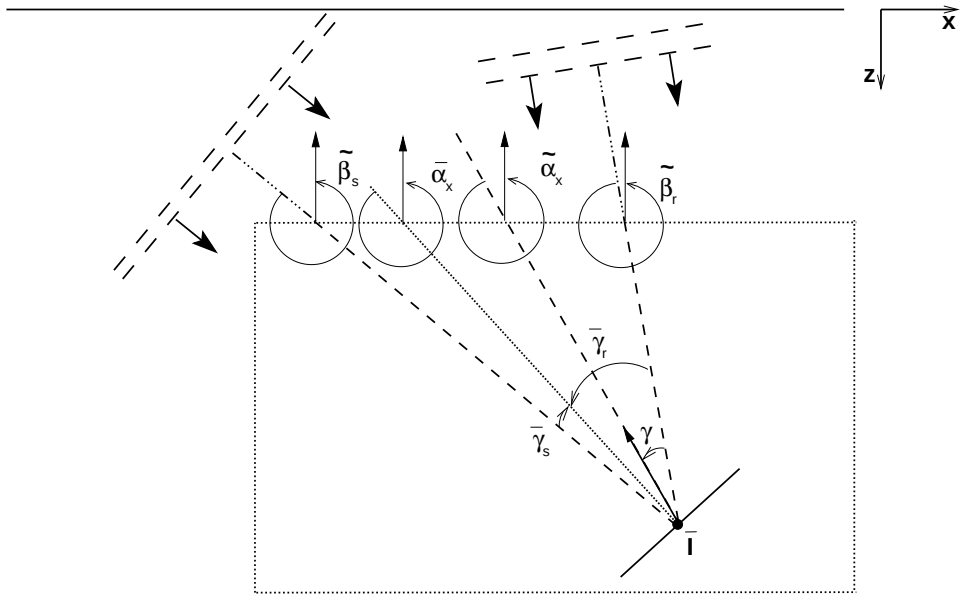


Figure 1: Sketch representing the reflection of a plane wave in an anisotropic medium. biondo1-cig-aniso-v2 [NR]

Figure 1 shows the geometric interpretation of these angles. Notice that the average dip angle $\widetilde{\alpha}_x$ is different from the true geological dip angle $\overline{\alpha}_x$, and that the average aperture angle $\widetilde{\gamma}$ is obviously different from the true aperture angles $\widetilde{\gamma}_s$ and $\widetilde{\gamma}_r$. However, the five angles are related and, if needed, the true angles can be derived from the average angles (Rosales and Biondi, 2005).

The transformation to the angle domain transforms the prestack image from the migrated subsurface offset domain $h_\xi$, to the angle domain by a slant stack transform. The transformation axis is thus the physical dip of the image along the subsurface offset; that is, $\partial z_\xi / \partial h_\xi$. The dip angles can be similarly related to the midpoint dips in the image; that is, $\partial z_\xi / \partial m_\xi$. Following the derivation of acoustic isotropic ADCIGs by Sava and Fomel (2003) and of converted-waves ADCIGs by Rosales and Rickett (2001), we can write the following relationships between the propagation angles and the derivative measured from the wavefield:

$$\left.\frac{\partial t}{\partial z_\xi}\right|_{(m_\xi=\overline{m}_\xi,\, h_\xi=\overline{h}_\xi)} = \widetilde{S}_s \cos(\widetilde{\alpha}_x - \widetilde{\gamma}) - \widetilde{S}_r \cos(\widetilde{\alpha}_x + \widetilde{\gamma}), \tag{9}$$

$$\left.\frac{\partial t}{\partial m_\xi}\right|_{(z_\xi=\overline{z}_\xi,\, h_\xi=\overline{h}_\xi)} = \widetilde{S}_s \sin(\widetilde{\alpha}_x - \widetilde{\gamma}) + \widetilde{S}_r \sin(\widetilde{\alpha}_x + \widetilde{\gamma}), \tag{10}$$

$$\left.\frac{\partial t}{\partial h_\xi}\right|_{(z_\xi=\overline{z}_\xi,\, m_\xi=\overline{m}_\xi)} = \widetilde{S}_s \sin(\widetilde{\alpha}_x - \widetilde{\gamma}) - \widetilde{S}_r \sin(\widetilde{\alpha}_x + \widetilde{\gamma}), \tag{11}$$

where $\widetilde{S}_s$ and $\widetilde{S}_r$ are the phase slownesses for the source and receiver wavefields, respectively. We obtain the expression for the offset dip by taking the ratio of equation 11 with equation 9, and similarly for the midpoint dips by taking the ratio of equation 10 with equation 9, and

after some algebraic manipulations, we obtain the following expressions:

$$\left.\frac{\partial z_\xi}{\partial h_\xi}\right|_{(m_\xi=\overline{m}_\xi)} = \frac{\tan\widetilde{\gamma}+\frac{\widetilde{S}_r-\widetilde{S}_s}{\widetilde{S}_r+\widetilde{S}_s}\tan\widetilde{\alpha}_x}{1-\frac{\widetilde{S}_r-\widetilde{S}_s}{\widetilde{S}_r+\widetilde{S}_s}\tan\widetilde{\alpha}_x\tan\widetilde{\gamma}}, \tag{12}$$

$$\left.\frac{\partial z_\xi}{\partial m_\xi}\right|_{(h_\xi=\overline{h}_\xi)} = \frac{\tan\widetilde{\alpha}_x+\frac{\widetilde{S}_r-\widetilde{S}_s}{\widetilde{S}_r+\widetilde{S}_s}\tan\widetilde{\gamma}}{1-\frac{\widetilde{S}_r-\widetilde{S}_s}{\widetilde{S}_r+\widetilde{S}_s}\tan\widetilde{\gamma}\tan\widetilde{\alpha}_x}. \tag{13}$$

In contrast with the equivalent relationships valid for isotropic media, these relationships depend on both the aperture angle $\widetilde{\gamma}$ and the dip angle $\widetilde{\alpha}_x$. The expression for the offset dip (equation 9) simplifies into the known relationship valid in isotropic media when either the difference between the phase slownesses is zero, or the dip angle $\widetilde{\alpha}_x$ is zero. In VTI media this happens for flat geological dips. In a general TI medium this condition is fulfilled when the geological dip is normal to the axis of symmetry.

Solving for $\tan\widetilde{\gamma}$ and $\tan\widetilde{\alpha}_x$ we obtain the following:

$$\tan\widetilde{\gamma} = \frac{\frac{\partial z_\xi}{\partial h_\xi}-\Delta_{\widetilde{S}}\tan\widetilde{\alpha}_x}{1+\frac{\partial z_\xi}{\partial h_\xi}\Delta_{\widetilde{S}}\tan\widetilde{\alpha}_x}, \tag{14}$$

$$\tan\widetilde{\alpha}_x = \frac{\frac{\partial z_\xi}{\partial m_\xi}-\Delta_{\widetilde{S}}\tan\widetilde{\gamma}}{1+\frac{\partial z_\xi}{\partial m_\xi}\Delta_{\widetilde{S}}\tan\widetilde{\gamma}}, \tag{15}$$

where for convenience I substituted the symbol $\Delta_{\widetilde{S}}$ for the "normalized slowness difference" $(\widetilde{S}_r-\widetilde{S}_s)/(\widetilde{S}_r+\widetilde{S}_s)$.

Substituting equation 15 in equation 14, and equation 14 into equation 15, we get the following two quadratic expressions that can be solved to estimate the angles as a function of the dips measured from the image:

$$\left[\frac{\partial z_\xi}{\partial m_\xi}\Delta_{\widetilde{S}}-\frac{\partial z_\xi}{\partial h_\xi}\Delta^2_{\widetilde{S}}\right]\tan^2\widetilde{\gamma}+\left[1-\Delta^2_{\widetilde{S}}\right]\tan\widetilde{\gamma}+\frac{\partial z_\xi}{\partial m_\xi}\Delta_{\widetilde{S}}-\frac{\partial z_\xi}{\partial h_\xi} = 0 \tag{16}$$

$$\left[\frac{\partial z_\xi}{\partial h_\xi}\Delta_{\widetilde{S}}-\frac{\partial z_\xi}{\partial m_\xi}\Delta^2_{\widetilde{S}}\right]\tan^2\widetilde{\alpha}_x+\left[1-\Delta^2_{\widetilde{S}}\right]\tan\widetilde{\alpha}_x+\frac{\partial z_\xi}{\partial h_\xi}\Delta_{\widetilde{S}}-\frac{\partial z_\xi}{\partial m_\xi} = 0 \tag{17}$$

These are two independent quadratic equations in $\tan\widetilde{\gamma}$ and $\tan\widetilde{\alpha}_x$ that can be solved independently. If the "normalized slowness difference" $\Delta_{\widetilde{S}}$ between the slowness along the propagation directions of the source and receiver wavefields are known, we can directly compute $\widetilde{\gamma}$ and $\widetilde{\alpha}_x$, and then the true $\widetilde{\beta}_s$ and $\widetilde{\beta}_r$. One important case in this category is when we image converted waves.

For anisotropic velocities, the slownesses depend on the propagation angles, and thus the normalized difference depends on the unknown $\widetilde{\gamma}$ and $\widetilde{\alpha}_x$. In practice, these equations can be solved by a simple iterative process that starts by assuming the "normalized difference" to be equal to zero. In all numerical test I conducted this iterative process converges to the correct solution in only a few iterations, and thus is not computationally demanding.

The dependency of equations 16 and 17 from the slowness function is also an impediment to the use of efficient Fourier-domain methods to perform the transformation to angle domain, because the slowness function cannot be assumed to be constant. Fortunately, the numerical examples shown below indicate that for practical values of the anisotropy parameters the dependency of the estimate from the dip angles can be safely ignored for small dips, and it is unlikely to constitute a problem for steep dips.

## KINEMATIC ANALYSIS OF ADCIGS BY INTEGRAL MIGRATION

The analysis shown in the previous section provides the fundamental equations to relate the offset and midpoint dips measured from prestack images to the phase angles at the reflection point. However, the previous analysis is not directly applicable to the analysis of residual moveout in the ADCIGs caused by velocity errors because it is based on plane waves and not rays. We are interested in relating traveltime errors accumulated during the propagation in the overburden to movements of the migrated events in the ADCIG; the traveltime errors are naturally evaluated along rays, which are related to group velocity and angles. To overcome this difficulty, in this section I introduce an integral formulation of the methodology to compute angle gathers that enables a simple link between ADCIGs and kinematics.

My analysis is based on the conceptual generalization of integral (Kirchhoff) migration to the computation of sub-surface offset gathers. Integral migration is defined by the summation surfaces over which the data are integrated to compute the image at every point in the image space. The shapes of these summation surfaces are usually computed as the sum of the time delays from the image point $(z_\xi, m_\xi)$ in the subsurface to the source and receiver locations at the surface. The basic idea underlying the generalization I introduce in this paper, is that we can compute the summation surfaces by evaluating the time delays starting not from the same point in the subsurface for both the source and receiver rays, but starting from two points horizontally shifted by $\pm h_\xi$ with respect to the image point. The summation of data along these surfaces produces a prestack image as a function of the subsurface offset that is kinematically equivalent to the image created by wavefield-continuation migrations such as source-receiver downward continuation, or shot-profile migration in conjunction to the generalized imaging condition discussed by Rickett and Sava (2002). Therefore, the kinematic analysis that follows, and its conclusions, are independent from the migration method applied to compute the prestack images. An interesting observation is that the ADCIGs computed using this generalization of integral migration should be immune from the artifacts that affect angle gathers computed by conventional integral migration and discussed by Stolk and Symes (2003).

### Generalized migration impulse response in parametric form

Integral migration can be conceptually performed by spreading the data along spreading surfaces as well as by summing data along the summation surfaces discussed above. The spreading surfaces are duals of the summation surfaces and represent the impulse response of the migration operator. In homogeneous anisotropic medium the shape of the impulse responses

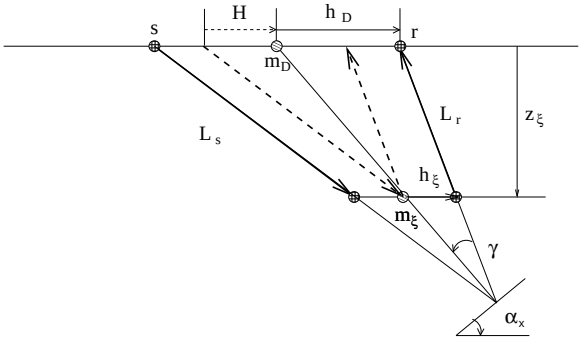


Figure 2: Geometry used for evaluating the impulse response of the generalized integral migration. biondo1-imp-resp [NR]

of the generalized integral migration can be easily evaluated analytically as a function of the subsurface offset $h_\xi$, in addition to the usual image depth $z_\xi$ and midpoint $m_\xi$. Figure 2 illustrates the geometry used to evaluate this impulse response. Notice that the angles in this figure ($\alpha_x$ and $\gamma$) are missing a tilde because they are group angles, and not phase angles as in the previous section. In an isotropic medium these angles are the dip and aperture angles, but in an anisotropic medium these angles are not easily related to the geological dip and the reflection aperture angles. They can be thought of as convenient parameters to evaluate the impulse response.

Simple trigonometry applied to Figure 2 allows us to express the impulse response in parametric form, as a function of $\alpha_x$ and $\gamma$. If we migrate an impulse recorded at time $t_D$, midpoint $m_D$ and surface offset $h_D$, the migration impulse response can be expressed as follows:

$$z_\xi = L(\alpha_x,\gamma)\frac{\cos^2\alpha_x-\sin^2\gamma}{\cos\alpha_x\cos\gamma}, \tag{18}$$

$$m_\xi = m_D - L(\alpha_x,\gamma)\frac{\sin\alpha_x}{\cos\gamma}, \tag{19}$$

$$h_\xi = h_D - H = h_D - L(\alpha_x,\gamma)\frac{\sin\gamma}{\cos\alpha_x}, \tag{20}$$

with

$$L(\alpha_x,\gamma) = \frac{L_s+L_r}{2}. \tag{21}$$

In a isotropic medium the half path-length $L$ would be simply given by $t_D/2S$, but in an anisotropic medium it is function of the angles. Its two components $L_s$ and $L_r$ can be calculated by solving the following system of linear equations:

$$t_D = S_s L_s + S_r L_r, \tag{22}$$

$$z_s - z_r = L_s\cos(\alpha_x-\gamma) - L_r\cos(\alpha_x+\gamma) = 0. \tag{23}$$

Equation 22 constraints the total traveltime to be equal to the impulse time, and equations 23 constraints the depth of the end point of the two rays ($z_s$ and $z_r$) to be equal, since the subsurface offset is assumed to be horizontal. The solution of this system of equation yields the following for the half path-length:

$$L(\alpha_x,\gamma) = \frac{L_s+L_r}{2} = \frac{t_D}{(S_r+S_s)+(S_r-S_s)\tan\alpha_x\tan\gamma}. \tag{24}$$

The combination of equation 24 and equations 18–20 enables the evaluation of the generalized migration impulse response in a arbitrary homogeneous anisotropic medium.

Figure 3 shows a 3-D rendering of the impulse response computed using the previous equations for an impulse with $t_D = .9$ seconds, $m_D = 0$ kilometers, and $h_D = .4$ kilometers, and vertical slowness $S_V = 1\ s/km$; the anisotropy parameters correspond to the Taylor Sand as listed in the table on page 80. The gray line (green in color) superimposed onto the impulse response is the result of cutting the surface at zero subsurface offset, and thus corresponds to the conventional impulse response of prestack migration. The black line superimposed onto the impulse response is the result of cutting the surface at zero midpoint. In Figure 4 these two lines are superimposed onto the corresponding vertical sections cut from the images computed by an anisotropic wavefield source-receiver migration applied with the same parameters described above. Figure 4b shows the conventional migration impulse response, whereas Figure 4a shows the zero-midpoint section. The lines computed by applying the kinematic equations perfectly match the impulse responses computed using wavefield migration, confirming the accuracy of the kinematic equations.

**Analytical evaluation of the tangent plane to the impulse response**

The expression for the generalized impulse response of prestack anisotropic migration leads to the analytical evaluation of the offset dip and midpoint dip along the planes tangent to the impulse response, as a function of the group angles and velocity. In this section I demonstrate that in the simple case of flat reflectors this analysis leads to exactly the same results as the phase-space analysis presented in the previous section. The derivation of the general relationships expressed in equations 13 and 12, which are valid for an arbitrary reflector's dip, is left to the reader.

By applying elementary analytical geometry, I demonstrate in Appendix A that the derivative of the depth with respect to the subsurface offset, at constant midpoint, is given by:

$$\left.\frac{\partial z_\xi}{\partial h_\xi}\right|_{m_\xi=\overline{m}_\xi} = -\frac{\frac{\partial z_\xi}{\partial \alpha_x}\frac{\partial m_\xi}{\partial \gamma} - \frac{\partial z_\xi}{\partial \gamma}\frac{\partial m_\xi}{\partial \alpha_x}}{\frac{\partial m_\xi}{\partial \alpha_x}\frac{\partial h_\xi}{\partial \gamma} - \frac{\partial m_\xi}{\partial \gamma}\frac{\partial h_\xi}{\partial \alpha_x}}, \tag{25}$$

and the derivative of the depth with respect to the midpoint, at constant subsurface offset, is given by:

$$\left.\frac{\partial z_\xi}{\partial m_\xi}\right|_{h_\xi=\overline{h}_\xi} = -\frac{\frac{\partial z_\xi}{\partial \alpha_x}\frac{\partial h_\xi}{\partial \gamma} - \frac{\partial z_\xi}{\partial \gamma}\frac{\partial h_\xi}{\partial \alpha_x}}{\frac{\partial m_\xi}{\partial \alpha_x}\frac{\partial h_\xi}{\partial \gamma} - \frac{\partial m_\xi}{\partial \gamma}\frac{\partial h_\xi}{\partial \alpha_x}}. \tag{26}$$

In the special case of flat reflectors the $\partial z_\xi/\partial \alpha_x$ and $\partial h_\xi/\partial \gamma$ vanish, and thus equation 25

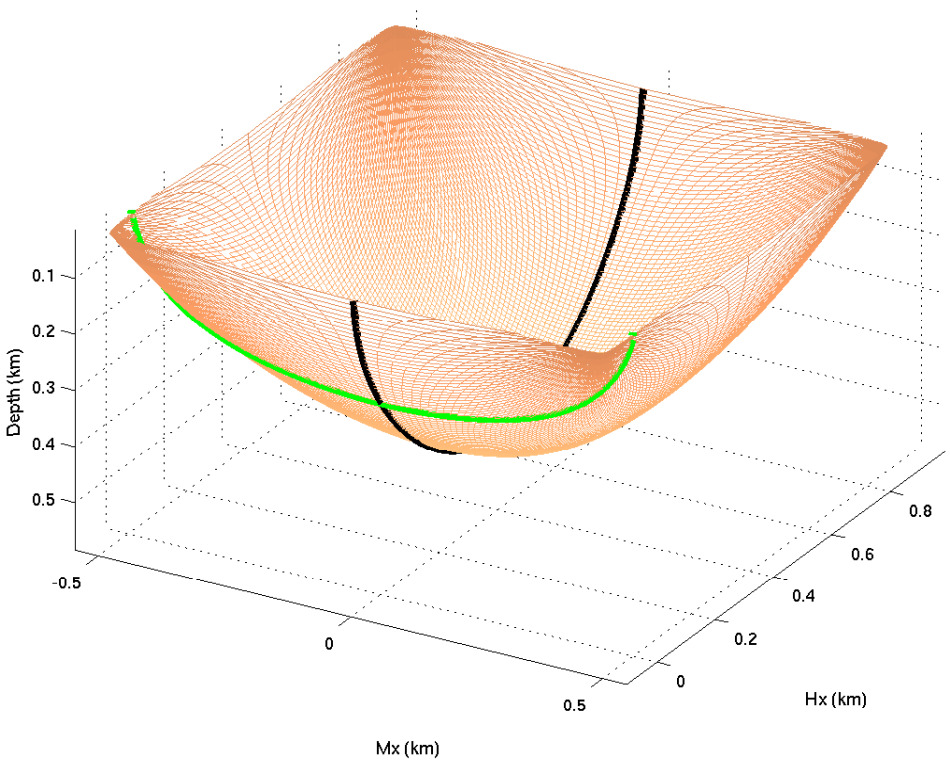


Figure 3: Impulse response of generalized anisotropic prestack migration. The gray line (green in color) superimposed onto the impulse response corresponds to the conventional impulse response of prestack migration. biondo1-surf_taylor_hxd_dot_4 [CR]

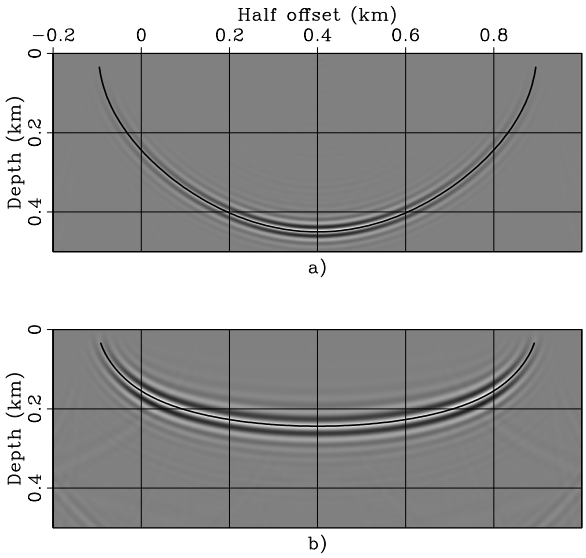


Figure 4: Vertical sections cut from the impulse response computed by an anisotropic wavefield source-receiver migration. The lines superimposed onto the images correspond to the lines superimposed onto the surface shown in Figure 3 and are computed by applying the kinematic expressions presented in equations 18–24. biondo1-Surf-taylor_hxd_.4-overn [CR]

simplifies into the following expression:

$$\left.\frac{\partial z_\xi}{\partial h_\xi}\right|_{(m_\xi=\overline{m}_\xi,\,\alpha_x=0)} = \frac{\left(\left.\frac{\partial z_\xi}{\partial \gamma}\right|_{L=\overline{L}} + \frac{\partial L}{\partial \gamma}\cos\gamma\right)\frac{\partial m_\xi}{\partial \alpha_x}}{\left(\left.\frac{\partial h_\xi}{\partial \gamma}\right|_{L=\overline{L}} - \frac{\partial L}{\partial \gamma}\sin\gamma\right)\frac{\partial m_\xi}{\partial \alpha_x}}$$

$$= \frac{\left.\frac{\partial z_\xi}{\partial \gamma}\right|_{L=\overline{L}} + \frac{\partial L}{\partial \gamma}\cos\gamma}{\left.\frac{\partial h_\xi}{\partial \gamma}\right|_{L=\overline{L}} - \frac{\partial L}{\partial \gamma}\sin\gamma}. \tag{27}$$

(28)

By substituting into equation 27 the appropriate derivative of the image coordinates and of the half path-length with respect to the angles, all provided in Appendix A, I further simplify the expression into the following:

$$\left.\frac{\partial z_\xi}{\partial h_\xi}\right|_{(m_\xi=\overline{m}_\xi,\,\alpha_x=0)} = \frac{\tan\gamma + \frac{1}{S}\frac{\partial S}{\partial \gamma}}{1 - \frac{1}{S}\frac{\partial S}{\partial \gamma}\tan\gamma}. \tag{29}$$

Finally, by applying the transformation from group angles into phase angles expressed in equation 4, I obtain the final result that for flat reflectors the subsurface-offset dip is exactly equal to the tangent of the phase aperture angle $\widetilde{\gamma}$; that is:

$$\left.\frac{\partial z_\xi}{\partial h_\xi}\right|_{(m_\xi=\overline{m}_\xi,\,\alpha_x=0)} = \tan\widetilde{\gamma}. \tag{30}$$

**Numerical examples of aperture angle along impulse responses**

The analytical kinematic results can be verified by numerical computations of impulse responses by wavefield migration and transformation of the resulting prestack image cubes into the angle domain. Figure 5 shows four zero subsurface-offset sections cut through the impulse responses computed by wavefield-continuation anisotropic migration for the three anisotropic rocks described in the table on page 80 and for an isotropic rock. The parameters defining the impulse responses are the same as for Figure 3; that is, $t_D = .9$ seconds, $m_D = 0$ kilometers, and $h_D = .4$ kilometers, and vertical slowness $S_V = 1\ s/km$. Figure 5a shows the isotropic case, Figure 5b shows the Taylor Sand case, Figure 5c shows the Mesa Clay Shale case, and Figure 5d shows the GreenLight River Shale case. As in Figure 4, the line superimposed onto the images represent the impulse response computed using the kinematic expressions in equations 18–24. The kinematic curves perfectly predicts the shape of the images even for very steep dips.

Figure 6 shows two-dimensional slices cut through the cube obtained by the transformation to the angle domain of the impulse responses shown in Figure 5. The slices are cut at the midpoint and depth corresponding to the expected location of the impulse responses; that is, at the location tracked by the lines shown in Figure 5. There are three lines superimposed onto the angle-domain images. The solid lines display the numerical computation of $\arctan(\partial z_\xi/\partial h_\xi)$ by applying equation 25. They perfectly track, as expected, the results of the transformation

of the prestack images to angle domain. The dotted lines display the phase aperture angle $\widetilde{\gamma}$. As expected, they overlap with the solid line around the zero midpoint (i.e. flat reflector), and depart from them at larger midpoints, which correspond to steeper reflections. However, the error introduced by ignoring the difference between $\arctan(\partial z_\xi / \partial h_\xi)$ and $\widetilde{\gamma}$ is small, and likely to be negligible in most practical situations. Finally, the dashed lines display the group aperture angle $\gamma$. The differences between $\gamma$ and $\widetilde{\gamma}$ are substantial, up to 20% in some cases. Ignoring them might be detrimental to the application of ADCIGs. Notice that in the isotropic case the three lines perfectly overlap and all of them match the image.

## ANISOTROPIC RESIDUAL MOVEOUT FOR FLAT REFLECTORS

The kinematic formulation of the generalized impulse response presented in the previous section enables a simple analysis of the residual moveout (RMO) in ADCIGs caused by errors in anisotropic velocity parameters. For the sake of simplicity, at the present, I limit my analysis to reflections from flat interfaces. However, a generalization of the flat-events analysis to dipping events should be conceptually straightforward, though not necessarily simple from the analytical point of view.

A VTI velocity function, either group or phase, is described by the following vector of three velocities $\mathbf{V} = (V_V, V_H, V_N)$, as for example used in equations 5, or by the corresponding vector of three slownesses $\mathbf{S} = (S_V, S_H, S_N)$ used in equation 6. I define the perturbations as one multiplicative factors for each of the velocities and one multiplicative factor for all velocities; that is, the perturbed velocity ${}_\rho\mathbf{V}$ is defined as:

$$ {}_\rho\mathbf{V} = \left({}_\rho V_V, {}_\rho V_H, {}_\rho V_N\right) = \rho_V \left(\rho_{V_V} V_V, \rho_{V_H} V_H, \rho_{V_N} V_N\right). \tag{31}$$

The velocity-parameter perturbations is thus defined by the following four-components vector $\boldsymbol{\rho} = \left(\rho_V, \rho_{V_V}, \rho_{V_H}, \rho_{V_N}\right)$.

For flat reflectors, the transformation to angle domain maps an image point at coordinates $(z_\xi, h_\xi)$ into an image point with coordinates $(z_\gamma, \widetilde{\gamma})$ according to the following mapping:

$$ \widetilde{\gamma} = \arctan \left.\frac{\partial z_\xi}{\partial h_\xi}\right|_{m_\xi = \overline{m}_\xi}, \tag{32}$$

$$ z_\gamma = z_\xi - h_\xi \left.\frac{\partial z_\xi}{\partial h_\xi}\right|_{m_\xi = \overline{m}_\xi} = z_\xi - h_\xi \tan\widetilde{\gamma}. \tag{33}$$

The partial derivative of the angle-domain depth $z_\gamma$ with respect to the $i$-th component in the perturbation vector can be expressed as follows:

$$\begin{aligned}
\frac{\partial z_\gamma}{\partial \rho_i} &= \frac{\partial z_\gamma}{\partial L}\frac{\partial L}{\partial \rho_i} + \frac{\partial z_\gamma}{\partial \gamma}\frac{\partial \gamma}{\partial \rho_i} + \frac{\partial z_\gamma}{\partial \widetilde{\gamma}}\frac{\partial \widetilde{\gamma}}{\partial \rho_i} \\
&= \frac{\partial z_\gamma}{\partial L}\frac{\partial L}{\partial S}\left(\frac{\partial S}{\partial \rho_i} + \frac{\partial S}{\partial \gamma}\frac{\partial \gamma}{\partial \rho_i}\right) + \frac{\partial z_\gamma}{\partial \gamma}\frac{\partial \gamma}{\partial \rho_i} + \frac{\partial z_\gamma}{\partial \widetilde{\gamma}}\frac{\partial \widetilde{\gamma}}{\partial \rho_i} \\
&= \frac{\partial z_\gamma}{\partial L}\frac{\partial L}{\partial S}\frac{\partial S}{\partial \rho_i} + \left(\frac{\partial z_\gamma}{\partial L}\frac{\partial L}{\partial S}\frac{\partial S}{\partial \gamma} + \frac{\partial z_\gamma}{\partial \gamma}\right)\frac{\partial \gamma}{\partial \rho_i} + \frac{\partial z_\gamma}{\partial \widetilde{\gamma}}\frac{\partial \widetilde{\gamma}}{\partial \rho_i}.
\end{aligned} \tag{34}$$

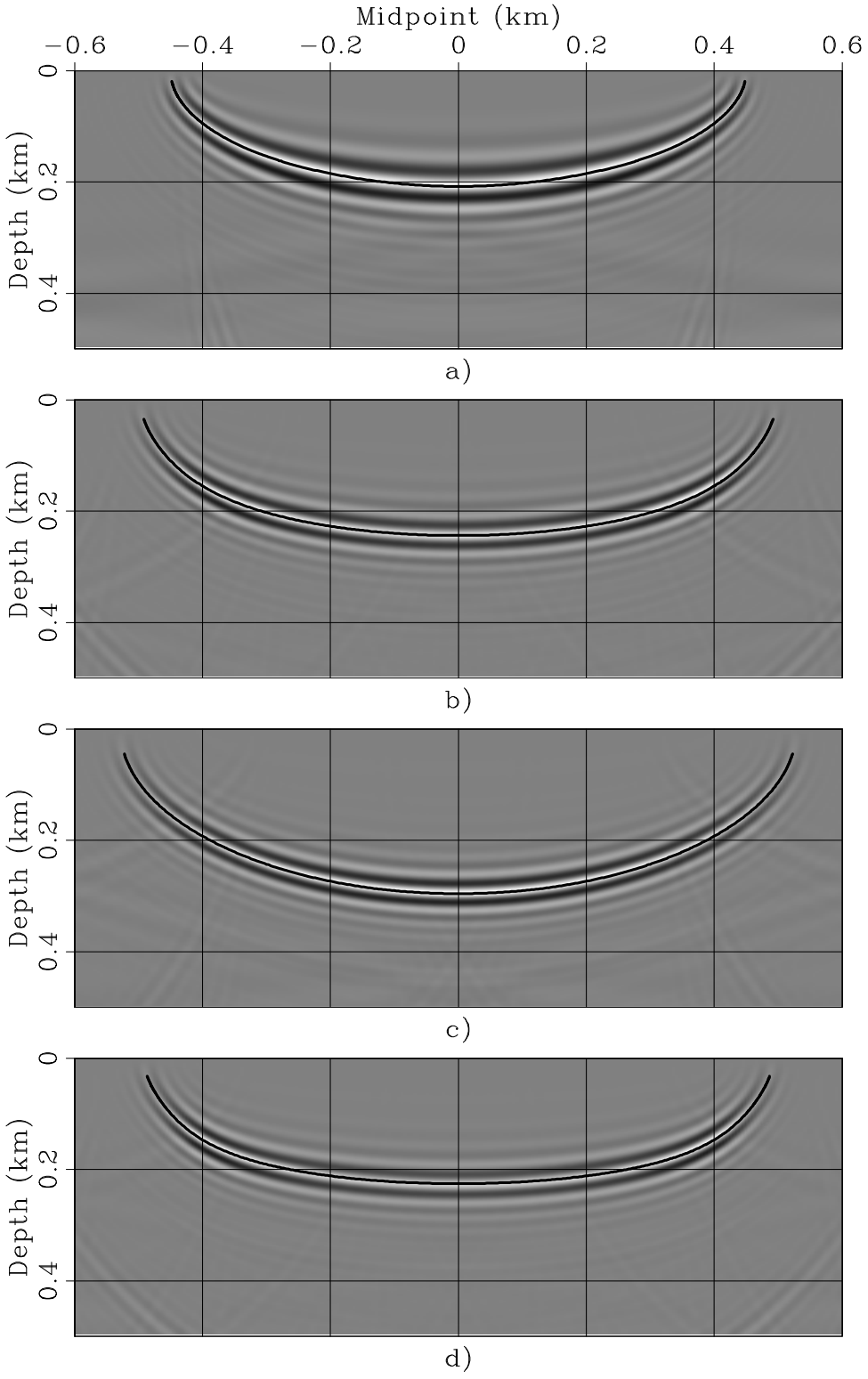


Figure 5: Impulse responses evaluated at zero subsurface offset for four rock types: a) Isotropic, b) Taylor Sand, c) Mesa Clay Shale, and d) GreenLight River Shale. Superimposed onto the images are the impulse responses computed by the kinematic expressions presented in equations 18–24. biondo1-Quad_hxd_.4-overn [CR]

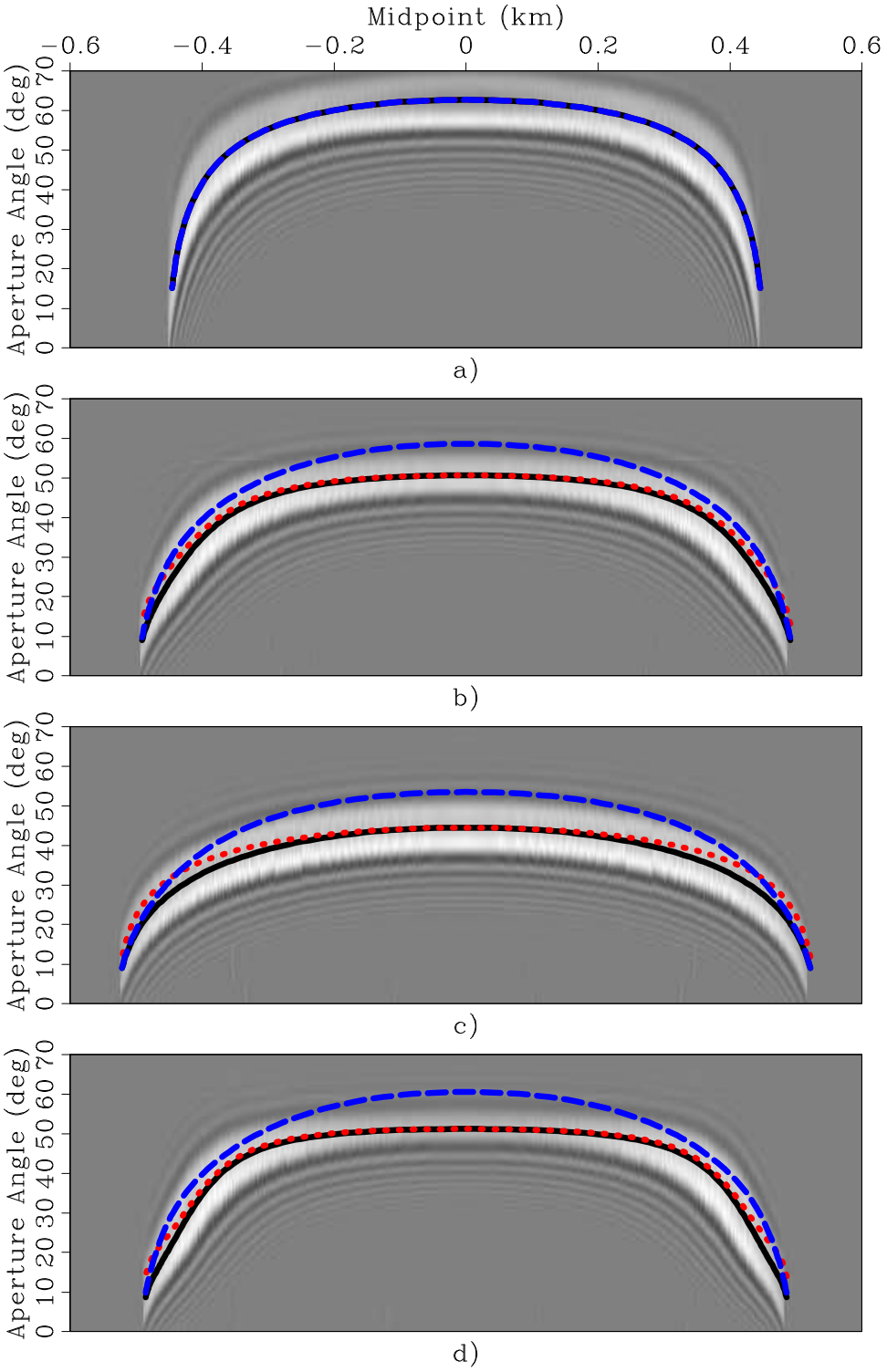


Figure 6: Slices of the impulse responses transformed into the angle-domain for four rock types: a) Isotropic, b) Taylor Sand, c) Mesa Clay Shale, and d) GreenLight River Shale. Superimposed onto the images there are the curves computed by applying the kinematic analysis: $\gamma$ (dashed line), $\widetilde{\gamma}$ (dotted line), and $\arctan(\partial z_\xi / \partial h_\xi)$ (solid line). biondo1-Quad_Mx-Ang_hxd_.4-overn [CR]

In Appendix B I demonstrate that the terms multiplying the partial derivatives with respect to the angles are zero, and equation 34 simplifies into:

$$\frac{\partial z_\gamma}{\partial \rho_i} = \frac{\partial z_\gamma}{\partial L}\frac{\partial L}{\partial S}\frac{\partial S}{\partial \rho_i}, \tag{35}$$

where

$$\frac{\partial z_\gamma}{\partial L} = \frac{\partial z_\xi}{\partial L} - \frac{\partial h_\xi}{\partial L}\tan\widetilde{\gamma} = \cos\gamma + \sin\gamma\tan\widetilde{\gamma}, \tag{36}$$

and

$$\frac{\partial L}{\partial S(\gamma)} = -\frac{z_\xi}{S(\gamma)\cos\gamma}, \tag{37}$$

**Uniform scaling of velocity**

The derivative with respect to the perturbation component $\rho_V$ has the following particularly simple form:

$$\frac{\partial z_\gamma}{\partial \rho_V} = z_\xi\,(1+\tan\gamma\tan\widetilde{\gamma}), \tag{38}$$

because the derivative of the slowness with respect to a uniform scaling of the velocity has the following simple form:

$$\frac{\partial S(\gamma)}{\partial \rho_V} = -S(\gamma), \tag{39}$$

that leads to the derivative $\partial L/\partial\rho_V$ to be independent from the "local" shape of the anisotropic slowness function. Intuitively, this simplification is related to the fact that the "shape" of the wavefronts is not affected by a uniform scaling of the velocity.

The residual moveout $\Delta z_{\mathrm{RMO}}$ is defined as the difference between the reflector movement at finite aperture angle $\widetilde{\gamma}$ and the reflector movement at normal incidence. From equation 38 the partial derivative of $\Delta z_{\mathrm{RMO}}$ with respect to $\rho_V$ is equal to the following expression:

$$\frac{\partial \Delta z_{\mathrm{RMO}}}{\partial \rho_V} = z_\xi\tan\gamma\tan\widetilde{\gamma}. \tag{40}$$

When the medium is isotropic, and the phase angles are equal to the group angles, the RMO expression in equation 40 becomes the RMO expression introduced by Biondi and Symes (2003). The dependency of equation 40 from the group angles makes its use in RMO analysis somewhat less convenient, because it requires the transformation of phase angles (measured directly from the image) into group angles by applying equation 1. The computational cost of evaluating equation 1 is negligible, but its use makes the computations dependent on the local values of the background anisotropic velocity function. On the other hand, the following numerical examples show that substantial errors are introduced when the distinction between

the group and phase angles is neglected, and the phase angle is used instead of the group angle in equation 40.

Figure 7 shows ADCIGs when an anisotropic velocity was perturbed by $\rho_V = .99$. The four panels correspond to four rock types: a) Isotropic, b) Taylor Sand, c) Mesa Clay Shale, and d) GreenLight River Shale. Superimposed onto the images are the RMO functions computed using equation 40. The solid line was computed by computing $\tan\gamma$ from $\tan\widetilde{\gamma}$ by applying equation 1, whereas the dashed line was computed by approximating $\tan\gamma$ as equal to $\tan\widetilde{\gamma}$. The RMO curves computed using the correct group angle perfectly match the residual moveout of the images. On the contrary, when the phase angles are used instead of the group angles, significant errors are introduced even for such a small perturbation in the parameters ($\rho_V = .99$). It is interesting to notice that the errors are larger for the rock types exhibiting strong unelliptical anisotropy (Taylors Sand and GreenLight River Shale) than for the strongly anisotropic but quasi-elliptical rock (Mesa Clay Shale).

The expression for the RMO function derived in equation 40 is based on a linearization, and thus when the the perturbations in velocity parameters are large it is not as accurate as it is when the perturbations are small (e.g. $\rho_V = .99$). Figure 8 illustrates this fact by showing a similar experiment as the one shown in Figure 7, but with a perturbation 10 times larger; that is, with $\rho_V = .9$. As in Figure 7, the four panels correspond to four rock types: a) Isotropic, b) Taylor Sand, c) Mesa Clay Shale, and d) GreenLight River Shale, and the lines superimposed onto the images are the RMO functions computed by using the correct values for $\tan\gamma$ (solid lines), and by using $\tan\widetilde{\gamma}$ in place of $\tan\gamma$ (dashed lines). With large perturbations, the predicted RMO functions differ from the actual RMO functions at wide aperture angles even when the correct values of the group angles are used in equation 40. However, even with such large perturbations the predicted RMO functions are still useful approximations of the actual RMO functions. In particular, it can be observed that the predicted RMO function correctly approximates the differences in shape of the actual RMO function among the rock types. These shape variations are related to the variations in shape of the wavefronts, which are reflected in the predicted RMO function through the variations in the mapping from phase angles to group angles.

**Arbitrary scaling of velocity**

The expressions of the derivative of $z_\gamma$ with respect to arbitrary perturbations of individual velocity components (i.e. $V_V$, $V_H$, and $V_N$) are slightly more complex than with respect to $\rho_V$ because the wavefronts are deformed when the velocity components are unevenly perturbed. These derivatives can be expressed as:

$$\frac{\partial z_\gamma}{\partial \rho_{V_V}} = -\frac{z_\xi}{S(\gamma)}\frac{\partial S(\gamma)}{\partial \rho_{V_V}}(1+\tan\gamma\tan\widetilde{\gamma}), \tag{41}$$

$$\frac{\partial z_\gamma}{\partial \rho_{V_H}} = -\frac{z_\xi}{S(\gamma)}\frac{\partial S(\gamma)}{\partial \rho_{V_H}}(1+\tan\gamma\tan\widetilde{\gamma}), \tag{42}$$

$$\frac{\partial z_\gamma}{\partial \rho_{V_N}}, = -\frac{z_\xi}{S(\gamma)}\frac{\partial S(\gamma)}{\partial \rho_{V_N}}(1+\tan\gamma\tan\widetilde{\gamma}). \tag{43}$$

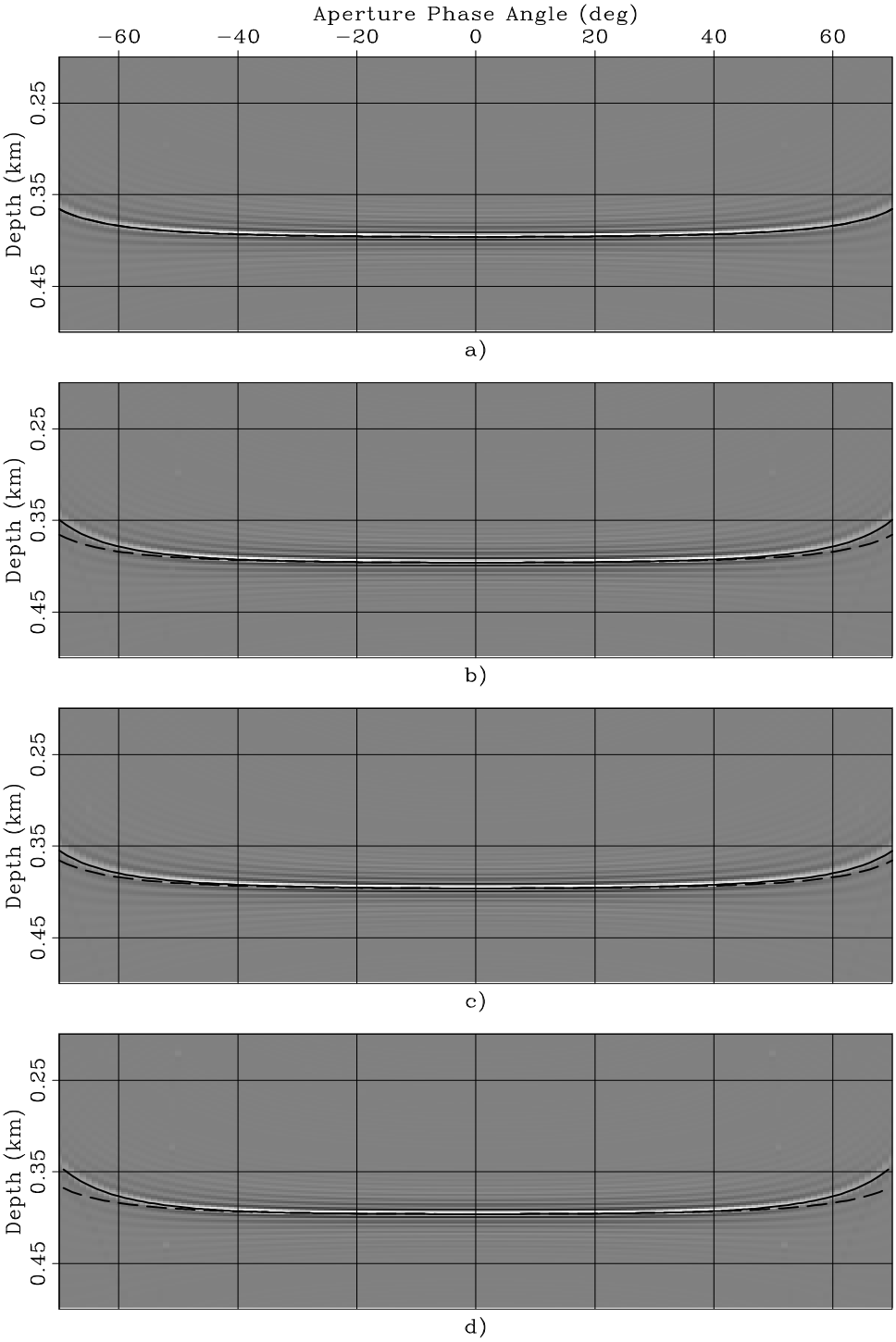


Figure 7: ADCIGs obtained when a constant anisotropic velocity was perturbed by $\rho_V = .99$ for four rock types: a) Isotropic, b) Taylor Sand, c) Mesa Clay Shale, and d) GreenLight River Shale. Superimposed onto the images are the RMO functions computed using equation 40. The solid line was computed when $\tan\gamma$ was derived from $\tan\widetilde{\gamma}$ by applying equation 1, whereas the dashed line was computed by approximating $\tan\gamma$ as equal to $\tan\widetilde{\gamma}$. biondo1-Quad_Aniso-rho.99_overn [CR]

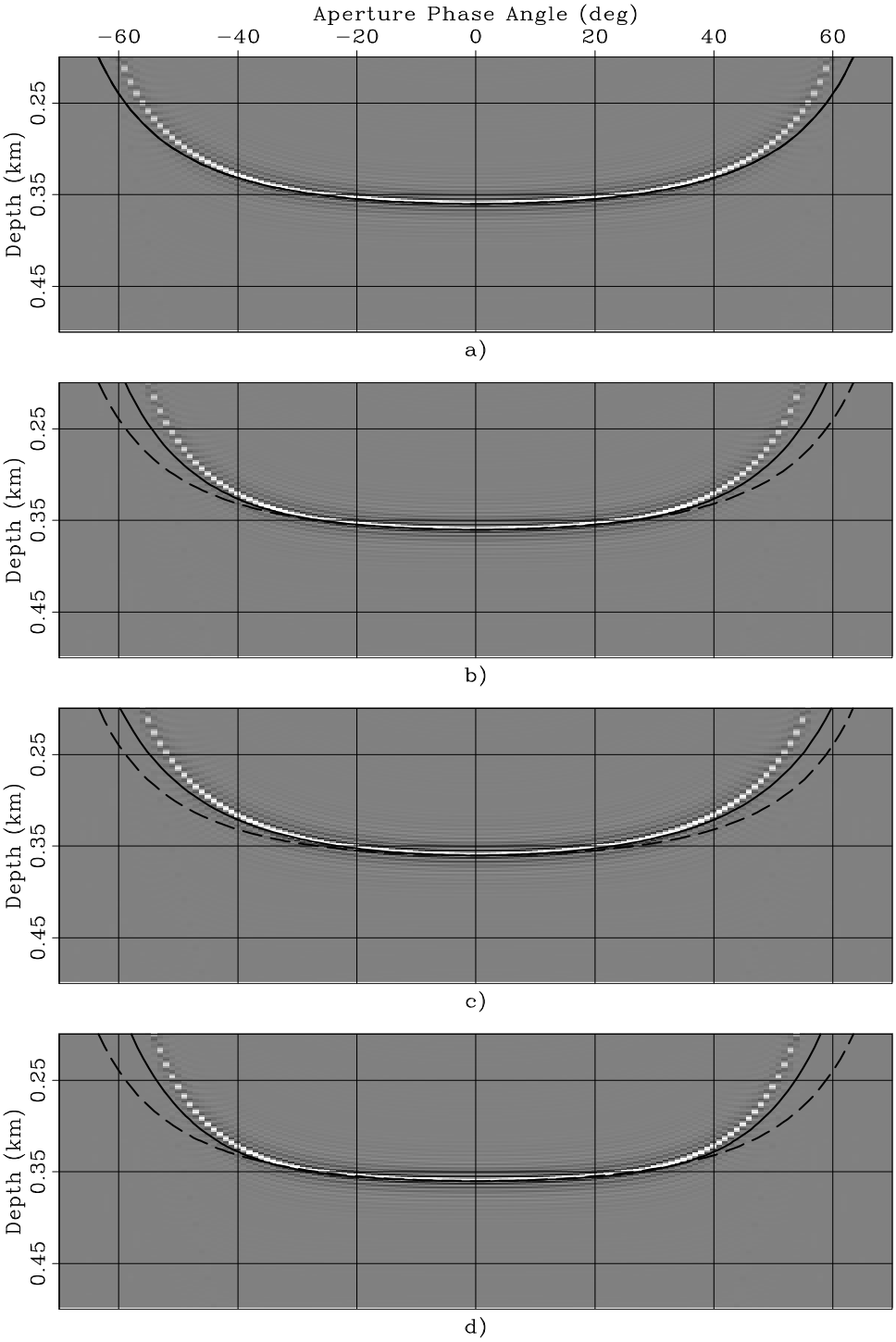


Figure 8: ADCIGs obtained when a constant anisotropic velocity was perturbed by $\rho_V = .9$ for four rock types: a) Isotropic, b) Taylor Sand, c) Mesa Clay Shale, and d) GreenLight River Shale. Superimposed onto the images are the RMO functions computed using equation 40. The solid line was computed when $\tan\gamma$ was derived from $\tan\widetilde{\gamma}$ by applying equation 1, whereas the dashed line was computed by approximating $\tan\gamma$ as equal to $\tan\widetilde{\gamma}$. biondo1-Quad_Aniso-rho.9_overn [CR]

The expressions for the derivatives of the slowness function with respect to the perturbation parameters depend on the particular form chosen to approximate the slowness function. Appendix C derives these derivative for the VTI group slowness function approximation expressed in equation 6, which I used for the numerical experiments shown in this paper.

The partial derivatives of the RMO function $\Delta z_{\text{RMO}}$ are directly derived from the partial derivatives of $z_\gamma$, taking into account that for flat reflectors only the vertical velocity component $V_V$ influences the image depth of normal incidence. The derivatives of $\Delta z_{\text{RMO}}$ can thus be written as follows:

$$\frac{\partial \Delta z_{\text{RMO}}}{\partial \rho_{V_V}} = -\frac{z_\xi}{S(\gamma)}\frac{\partial S(\gamma)}{\partial \rho_{V_V}}(1+\tan\gamma\tan\widetilde{\gamma})-z_\xi, \tag{44}$$

$$\frac{\partial \Delta z_{\text{RMO}}}{\partial \rho_{V_H}} = -\frac{z_\xi}{S(\gamma)}\frac{\partial S(\gamma)}{\partial \rho_{V_H}}(1+\tan\gamma\tan\widetilde{\gamma}), \tag{45}$$

$$\frac{\partial \Delta z_{\text{RMO}}}{\partial \rho_{V_N}} = -\frac{z_\xi}{S(\gamma)}\frac{\partial S(\gamma)}{\partial \rho_{V_N}}(1+\tan\gamma\tan\widetilde{\gamma}). \tag{46}$$

Figures 9 and 10 show examples of the application of the generalized RMO functions expressed in equations 44–46. As in Figures 7– 8, I show the ADCIGs for three different anisotropic rock types, but, differently from the previous figures, not for the isotropic case. The order of the rock types is the same as in Figures 7– 8; that is: panels a) correspond to Taylor Sand, panels b) to Mesa Clay Shale, and panels c) to GreenLight River Shale. Furthermore, as in Figures 7– 8, one figure (Figure 10) shows the ADCIG obtained with a smaller perturbation than the ADCIGs shown in the other figure (Figure 9). The ADCIGs shown in Figure 9 were obtained by performing *isotropic* migration on the synthetic data modeled assuming *anisotropic* velocity. The ADCIGs shown in Figure 10 were computed by scaling by .25 the parameter perturbations used to compute Figure 9. The lines superimposed onto the images are the RMO functions computed by using the correct values for $\tan\gamma$ (solid lines), and by using $\tan\widetilde{\gamma}$ in place of $\tan\gamma$ (dashed lines).

The predicted RMO functions accurately track the actual RMO functions when the parameter perturbations are sufficiently small to be within the range of accuracy of the linearization at the basis of the derivation of equation 40 (Figure 10). But even when the perturbations are large (Figure 9) and cause a substantial RMO (up to 30% of the reflector depth) the predicted RMO functions are excellent approximations of the actual RMO functions.

The RMO functions associated with the two strongly unelliptical rocks (Taylor Sand and GreenLight River Shale) exhibit a characteristic oscillatory behavior; the events at narrow-aperture angles are imaged deeper than the normal incidence event, whereas the events at wide-aperture angles are imaged shallower. This oscillatory behavior is well predicted by the analytical RMO function introduced in equations 44–46.

In contrast, the approximation of the group angles with the phase angles (dashed lines in the figures) seriously deteriorates the accuracy of the predicted RMO functions. Notice that, in contrast with the uniform perturbation case illustrated in Figures 7– 8, the dashed lines are different among the panels, because the derivatives of the slowness function with respect to the perturbation parameters depend on the anisotropic parameters of the background medium.

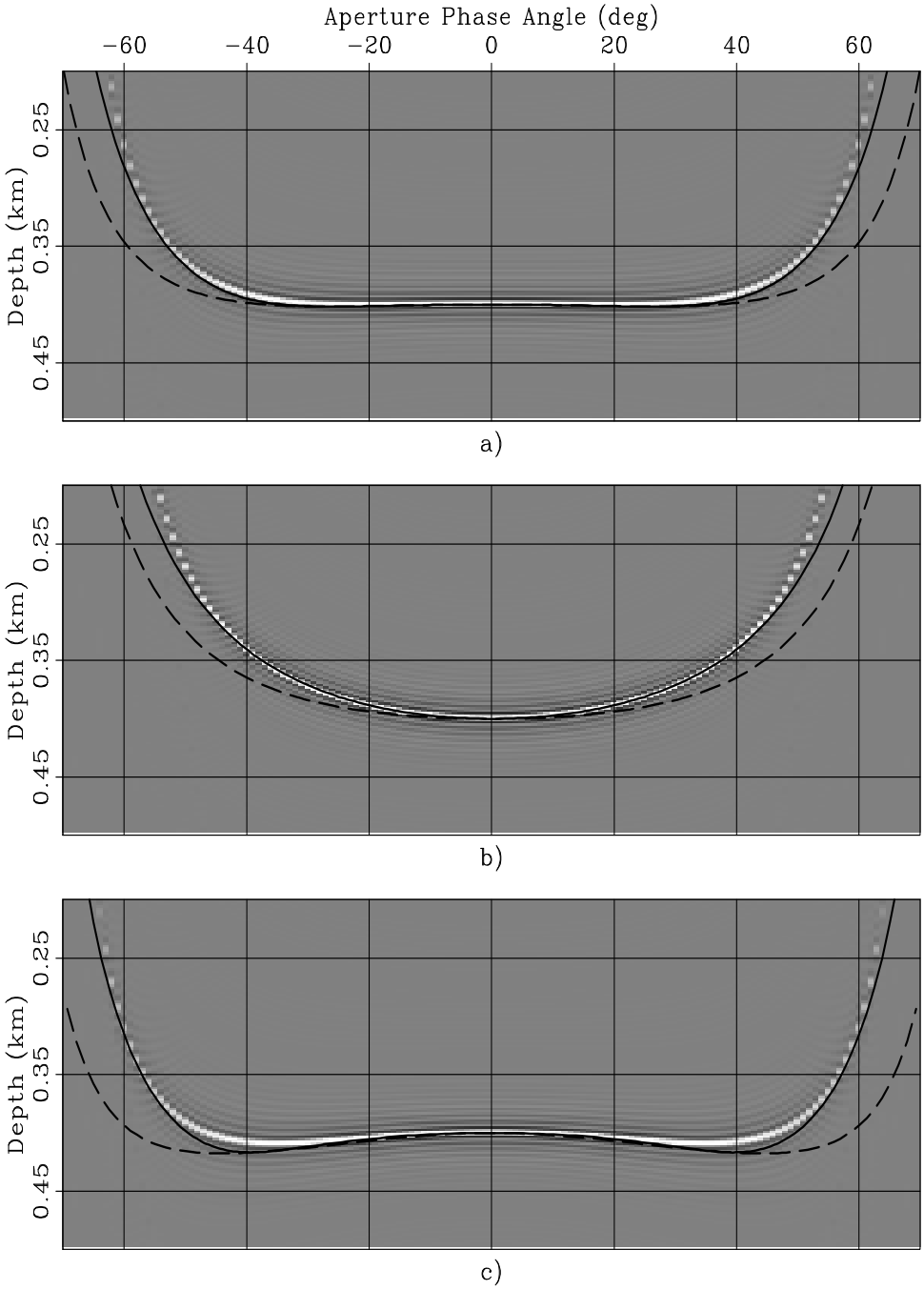


Figure 9: ADCIGs obtained when data modeled with an *anisotropic* velocity have been migrated using an *isotropic* velocity. The anisotropic data were modeled assuming three rock types: a) Taylor Sand, b) Mesa Clay Shale, and c) GreenLight River Shale. Superimposed onto the images are the RMO functions computed using equation 40. The solid line was computed when $\tan\gamma$ was derived from $\tan\widetilde{\gamma}$ by applying equation 1, whereas the dashed line was computed by approximating $\tan\gamma$ as equal to $\tan\widetilde{\gamma}$. biondo1-Trio_Aniso-iso_overn [CR]

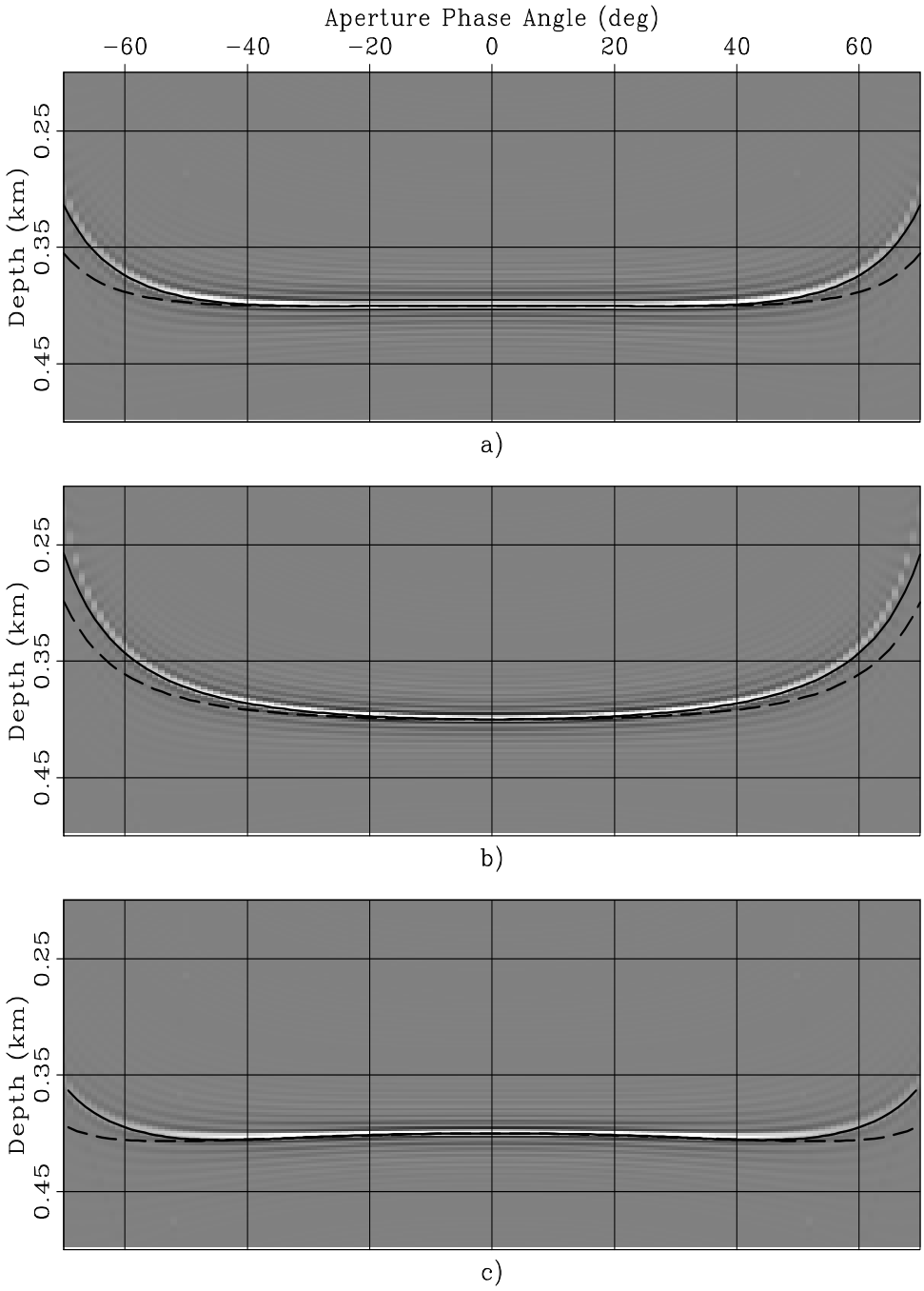


Figure 10: ADCIGs obtained when data modeled with an *anisotropic* velocity have been migrated using a *less anisotropic* velocity; that is, with anisotropic parameters obtained by scaling by .25 the parameter perturbations used to compute Figure 9. The anisotropic data were modeled assuming three rock types: a) Taylor Sand, b) Mesa Clay Shale, and c) Green-Light River Shale. Superimposed onto the images are the RMO functions computed using equation 40. The solid line was computed when $\tan\gamma$ was derived from $\tan\widetilde{\gamma}$ by applying equation 1, whereas the dashed line was computed by approximating $\tan\gamma$ as equal to $\tan\widetilde{\gamma}$. biondo1-Trio_Aniso-scaled_overn [CR]

### Conversion of depth errors into traveltime errors

The RMO functions derived above can be directly used in a layered-based vertical updating of the velocity function after migration. However, in complex media it is often desirable to invert the depth errors measured from ADCIGs into velocity-parameters perturbations through a tomographic procedure. To be able to apply a tomographic method, we must perform an additional step to convert the depth errors measured from ADCIGs into traveltime errors. This depth-to-time conversion can be easily accomplished by slightly rewriting the chain of partial derivatives in equation 35, and obtain the following relationship:

$$\frac{\partial z_\gamma}{\partial t} = \frac{\partial z_\gamma}{\partial L}\frac{\partial L}{\partial t} = \frac{\cos\gamma + \sin\gamma \tan\widetilde{\gamma}}{S(\gamma)}, \tag{47}$$

which can be directly applied to convert depth errors into traveltime perturbations to be used in tomography.

## CONCLUSIONS

The methodology for computing and analyzing ADCIGs that has been recently developed for isotropic media can be generalized to prestack images computed using anisotropic prestack migration. The transformation to angle domain performed by slant-stacking the subsurface-offset axis generates angle gathers that are approximately function of the phase aperture angle. In VTI media the approximation is exact for flat reflectors, and even for dipping reflectors it seems to be sufficiently accurate for practical applications with realistic anisotropic parameters.

The linearized analysis of ADCIGs obtained by anisotropic migration shows that the RMO function observed when the migration velocity is inaccurate is function of both the phase aperture angle and the group aperture angle. The numerical examples show that the linearized expression of the RMO function accurately predicts the actual RMO function measured after wavefield migration.

A simple modification of the analysis that yields the expression of the RMO function leads also to a linearized relationship between depth errors measured in ADCIGs and traveltime errors accumulated along the wavepaths. This relationship should enable the development of migration velocity analysis methods based on tomographic velocity-updating procedures.

## REFERENCES

Bear, L., Dickens, T., and Traynin, P. Incorporating nonseismic information for improved imaging with anisotropic PSDM:, 2003.

Biondi, B., and Sava, P., 1999, Wave-equation migration velocity analysis: 69th Ann. Internat. Meeting, Soc. of Expl. Geophys., Expanded Abstracts, 1723–1726.

Biondi, B., and Symes, W. W., 2003, Angle-domain common-image gathers for migration velocity analysis by wavefield-continuation imaging: Geophysics, **69**, 1283–1298.

Biondi, B., and Tisserant, T., 2004, 3-D angle-domain common-image gathers for migration velocity analysis: Geophisical Prospecting, **52**, 575–591.

Clapp, R., and Biondi, B., 2000, Tau domain migration velocity analysis using angle CRP gathers and geologic constrains: 70th Ann. Internat. Meeting, Soc. of Expl. Geophys., 926–929.

Dellinger, J., and Muir, F., 1985, Two domains of anisotropy: SEP–**44**, 59–62.

Fowler, P., 2003, Practical VTI approximations: a systematic anatomy: Journal of Applied Geophysics, **69**, 347–367.

Prucha, M., Biondi, B., and Symes, W. W., 1999, Angle-domain common-image gathers by wave-equation migration: 69th Ann. Internat. Meeting, Soc. Expl. Geophys., Expanded Abstracts, 824–827.

Rickett, J., and Sava, P., 2002, Offset and angle-domain common image-point gathers for shot-profile migration: Geophysics, **67**, 883–889.

Rosales, D. A., and Biondi, B., 2005, Converted-mode angle-domain common-image gathers for migration velocity analysis: SEP–**120**, 283–296.

Rosales, D., and Rickett, J., 2001, *ps*-wave polarity reversal in angle domain common-image gathers: SEP–**108**, 35–44.

Sarkar, D., and Tsvankin, I., 2003, Analysis of image gathers in factorized vti media: Geophysics, **68**, 2016–2025.

Sarkar, D., and Tsvankin, I. Anisotropic migration velocity analysis: Application to a data set from West Africa:, 2004.

Sarkar, D., and Tsvankin, I., 2004b, Migration velocity analysis in factorized vti media: Geophysics, **69**, 708–718.

Sava, P., and Fomel, S., 2003, Angle-domain common-image gathers by wavefield continuation methods: Geophysics, **68**, 1065–1074.

Sen, S., and Biondi, B., 2005, Common azimuth migration for elliptical and VTI media: SEP–**120**, 125–136.

Shan, G., and Biondi, B., 2005a, 3D wavefield extrapolation in laterally-varying tilted TI media: SEP–**120**, 105–124.

Shan, G., and Biondi, B., 2005b, Imaging steeply dipping reflectors in TI media by wavefield extrapolation: SEP–**120**, 63–76.

Stolk, C. C., and Symes, W. W., 2003, Kinematic artifacts in prestack depth migration: Geophysics: accepted for publication, **69**, 562–575.

Tsvankin, I., 2001, Seismic signatures and analysis of reflection data in anisotropic media: Elsevier Science.

## APPENDIX A - ANALYTICAL EVALUATION OF THE TANGENT PLANE TO THE IMPULSE RESPONSE

In this appendix I derive the expressions for evaluating the derivatives of image depth $z_\xi$ with respect to the subsurface offset $h_\xi$ and the midpoint $m_\xi$; these derivatives are computed along the tangent plane to the impulse response of the generalized migration operator, which is defined in equations 18–24.

I start by deriving the equation for the vector normal to the impulse-response surface, $\vec{n}$:

$$\begin{aligned}\vec{n} &= \begin{vmatrix} \vec{z}_\xi & \vec{m}_\xi & \vec{h}_\xi \\ \frac{\partial z_\xi}{\partial \alpha_x} & \frac{\partial m_\xi}{\partial \alpha_x} & \frac{\partial h_\xi}{\partial \alpha_x} \\ \frac{\partial z_\xi}{\partial \gamma} & \frac{\partial m_\xi}{\partial \gamma} & \frac{\partial h_\xi}{\partial \gamma} \end{vmatrix} \\ &= \left(\frac{\partial m_\xi}{\partial \alpha_x}\frac{\partial h_\xi}{\partial \gamma} - \frac{\partial m_\xi}{\partial \gamma}\frac{\partial h_\xi}{\partial \alpha_x}\right)\vec{z}_\xi + \left(-\frac{\partial z_\xi}{\partial \alpha_x}\frac{\partial h_\xi}{\partial \gamma} + \frac{\partial z_\xi}{\partial \gamma}\frac{\partial h_\xi}{\partial \alpha_x}\right)\vec{m}_\xi + \left(\frac{\partial z_\xi}{\partial \alpha_x}\frac{\partial m_\xi}{\partial \gamma} - \frac{\partial z_\xi}{\partial \gamma}\frac{\partial m_\xi}{\partial \gamma}\right)\vec{h}_\xi,\end{aligned} \tag{48}$$

where $\vec{z}_\xi$, $\vec{m}_\xi$, and $\vec{h}_\xi$ are respectively the unit vectors along the three dimensions $z_\xi$, $m_\xi$, and $h_\xi$.

The equation of the tangent plane at the image point with coordinates $\left(\overline{z}_\xi, \overline{m}_\xi, \overline{h}_\xi\right)$ is given by:

$$\begin{aligned} T\left(z_\xi, m_\xi, h_\xi\right) &= \left(\frac{\partial m_\xi}{\partial \alpha_x}\frac{\partial h_\xi}{\partial \gamma} - \frac{\partial m_\xi}{\partial \gamma}\frac{\partial h_\xi}{\partial \alpha_x}\right)\left(z_\xi - \overline{z}_\xi\right) \\ &+ \left(-\frac{\partial z_\xi}{\partial \alpha_x}\frac{\partial h_\xi}{\partial \gamma} + \frac{\partial z_\xi}{\partial \gamma}\frac{\partial h_\xi}{\partial \alpha_x}\right)\left(m_\xi - \overline{m}_\xi\right) \\ &+ \left(\frac{\partial z_\xi}{\partial \alpha_x}\frac{\partial m_\xi}{\partial \gamma} - \frac{\partial z_\xi}{\partial \gamma}\frac{\partial m_\xi}{\partial \alpha_x}\right)\left(h_\xi - \overline{h}_\xi\right) = 0. \end{aligned} \tag{49}$$

The derivative of the depth with respect o the subsurface offset, at constant midpoint, is given by:

$$\left.\frac{\partial z_\xi}{\partial h_\xi}\right|_{m_\xi = \overline{m}_\xi} = -\frac{\left.\frac{\partial T}{\partial h_\xi}\right|_{m_\xi = \overline{m}_\xi}}{\left.\frac{\partial T}{\partial z_\xi}\right|_{m_\xi = \overline{m}_\xi}} = -\frac{\frac{\partial z_\xi}{\partial \alpha_x}\frac{\partial m_\xi}{\partial \gamma} - \frac{\partial z_\xi}{\partial \gamma}\frac{\partial m_\xi}{\partial \alpha_x}}{\frac{\partial m_\xi}{\partial \alpha_x}\frac{\partial h_\xi}{\partial \gamma} - \frac{\partial m_\xi}{\partial \gamma}\frac{\partial h_\xi}{\partial \alpha_x}}. \tag{50}$$

and similarly the derivative of the depth with respect to the midpoint, at constant subsurface offset, is given by:

$$\left.\frac{\partial z_\xi}{\partial m_\xi}\right|_{h_\xi=\overline{h}_\xi} = -\frac{\left.\frac{\partial T}{\partial m_\xi}\right|_{h_\xi=\overline{h}_\xi}}{\left.\frac{\partial T}{\partial z_\xi}\right|_{h_\xi=\overline{h}_\xi}} = -\frac{\frac{\partial z_\xi}{\partial \alpha_x}\frac{\partial h_\xi}{\partial \gamma}-\frac{\partial z_\xi}{\partial \gamma}\frac{\partial h_\xi}{\partial \alpha_x}}{\frac{\partial m_\xi}{\partial \alpha_x}\frac{\partial h_\xi}{\partial \gamma}-\frac{\partial m_\xi}{\partial \gamma}\frac{\partial h_\xi}{\partial \alpha_x}}. \tag{51}$$

To evaluate equations 50–51. we need to evaluate the following partial derivatives, obtained by differentiating the expressions in equations 18–20:

$$\begin{aligned}
\frac{\partial z_\xi}{\partial \alpha_x} &= -L(\alpha_x,\gamma)\frac{\tan\alpha_x}{\cos\alpha_x\cos\gamma}\left(\cos^2\alpha_x+\sin^2\gamma\right)+\frac{\partial L(\alpha_x,\gamma)}{\partial \alpha_x}\frac{\cos^2\alpha_x-\sin^2\gamma}{\cos\alpha_x\cos\gamma},\\
\frac{\partial z_\xi}{\partial \gamma} &= -L(\alpha_x,\gamma)\frac{\tan\gamma}{\cos\alpha_x\cos\gamma}\left(\cos^2\gamma+\sin^2\alpha_x\right)+\frac{\partial L(\alpha_x,\gamma)}{\partial \gamma}\frac{\cos^2\alpha_x-\sin^2\gamma}{\cos\alpha_x\cos\gamma},\\
\frac{\partial m_\xi}{\partial \alpha_x} &= -L(\alpha_x,\gamma)\frac{\cos\alpha_x}{\cos\gamma}-\frac{\partial L(\alpha_x,\gamma)}{\partial \alpha_x}\frac{\sin\alpha_x}{\cos\gamma},\\
\frac{\partial m_\xi}{\partial \gamma} &= -L(\alpha_x,\gamma)\frac{\sin\gamma\sin\alpha_x}{\cos^2\gamma}-\frac{\partial L(\alpha_x,\gamma)}{\partial \gamma}\frac{\sin\alpha_x}{\cos\gamma},\\
\frac{\partial h_\xi}{\partial \alpha_x} &= -L(\alpha_x,\gamma)\frac{\sin\gamma\sin\alpha_x}{\cos^2\alpha_x}-\frac{\partial L(\alpha_x,\gamma)}{\partial \alpha_x}\frac{\sin\gamma}{\cos\alpha_x},\\
\frac{\partial h_\xi}{\partial \gamma} &= -L(\alpha_x,\gamma)\frac{\cos\gamma}{\cos\alpha_x}-\frac{\partial L(\alpha_x,\gamma)}{\partial \gamma}\frac{\sin\gamma}{\cos\alpha_x}.
\end{aligned} \tag{52}$$

The derivative of path length are evaluated as following:

$$\begin{aligned}
\frac{\partial L}{\partial \alpha_x} &= \frac{-t_D}{\left[(S_r+S_s)+(S_r-S_s)\tan\alpha_x\tan\gamma\right]^2}\\
&\left[\left(\frac{\partial S_r}{\partial \alpha_x}+\frac{\partial S_s}{\partial \alpha_x}\right)+\left(\frac{\partial S_r}{\partial \alpha_x}-\frac{\partial S_s}{\partial \alpha_x}\right)\tan\alpha_x\tan\gamma+\frac{(S_r-S_s)\tan\gamma}{\cos^2\alpha_x}\right],
\end{aligned} \tag{53}$$

and

$$\begin{aligned}
\frac{\partial L}{\partial \gamma} &= \frac{-t_D}{\left[(S_r+S_s)+(S_r-S_s)\tan\alpha_x\tan\gamma\right]^2}\\
&\left[\left(\frac{\partial S_r}{\partial \gamma}+\frac{\partial S_s}{\partial \gamma}\right)+\left(\frac{\partial S_r}{\partial \gamma}-\frac{\partial S_s}{\partial \gamma}\right)\tan\alpha_x\tan\gamma+\frac{(S_r-S_s)\tan\alpha_x}{\cos^2\gamma}\right].
\end{aligned} \tag{54}$$

**Application to the isotropic case**

The application to the isotropic case is simpler than the anisotropic case because the derivative of the path length is zero, but it is instructive since it verifies known results through a completely different derivation. Substituting equations 52 into equation 50, I obtain:

$$\begin{aligned}
\left.\frac{\partial z_\xi}{\partial h_\xi}\right|_{m_\xi=\overline{m}_\xi} &= -\frac{L^2\tan\gamma\left[\frac{\tan^2\alpha_x}{\cos^2\gamma}\left(\cos^2\alpha_x+\sin^2\gamma\right)-\frac{1}{\cos^2\gamma}\left(\cos^2\gamma+\sin^2\alpha_x\right)\right]}{L^2\left[1-\tan^2\alpha_x\tan^2\gamma\right]}\\
&= -\frac{L^2\tan\gamma\left[-1+\sin^2\alpha_x\left(\frac{1}{\cos^2\gamma}-\frac{1}{\cos^2\gamma}\right)+\tan^2\alpha_x\tan^2\gamma\right]}{L^2\left[1-\tan^2\alpha_x\tan^2\gamma\right]}\\
&= \tan\gamma,
\end{aligned} \tag{55}$$

which shows that $\partial z_\xi / \partial h_\xi$ is independent from the dip angle $\alpha_x$. This expression is consistent with the 2-D analysis by Sava and Fomel (2003) and the 3-D analysis by by Biondi and Tisserant (2004).

## APPENDIX B

In this appendix I demonstrate that the terms in equation 34 multiplying the partial derivatives with respect to the angles; that is, $\partial\gamma/\partial\rho_i$ and $\partial\widetilde{\gamma}/\partial\rho_i$, are zero when evaluated at the point when the events are correctly migrated at zero subsurface offset. We are interested in estimating the RMO function measured for an incorrect velocity. That RMO function can be seen as a perturbation around the image obtained with the correct velocity.

After simple evaluation of partial derivatives the term multiplying $\partial\gamma/\partial\rho_i$ in equation 34 can be written as the following:

$$\begin{aligned}\left(\frac{\partial z_\gamma}{\partial L}\frac{\partial L}{\partial S(\gamma)}\frac{\partial S(\gamma)}{\partial \gamma}+\frac{\partial z_\gamma}{\partial \gamma}\right) &= -\frac{z_\xi\,(\cos\gamma+\sin\gamma\tan\widetilde{\gamma})}{S(\gamma)\cos\gamma}\frac{\partial S(\gamma)}{\partial\gamma}-L\,(\sin\gamma-\cos\gamma\tan\widetilde{\gamma}) \\ &= -z_\xi\left[(1+\tan\gamma\tan\widetilde{\gamma})\frac{\partial S(\gamma)}{\partial\gamma}+\tan\gamma-\tan\widetilde{\gamma}\right], \qquad (56)\end{aligned}$$

that can be easily demonstrated to be equal to zero after substitution of the relationship between phase angles and group angles presented in equation 4.

The term multiplying $\partial\widetilde{\gamma}/\partial\rho_i$ is equal to

$$\frac{\partial z}{\partial\widetilde{\gamma}} = -h_\xi\frac{1}{\cos^2\widetilde{\gamma}}, \qquad (57)$$

which is obviously equal to zero when the subsurface offset is zero, the point around which we are interested in expanding the RMO function.

## APPENDIX C - DERIVATIVES OF VTI SLOWNESS FUNCTION WITH RESPECT TO THE PERTURBATION PARAMETERS

In this Appendix I present the analytical expressions for the derivatives of the VTI group slowness function expressed in equation 6 in the main text. These derivatives are necessary for the numerical computation of the RMO functions.

The VTI slowness function can be approximated as (Fowler, 2003):

$$\begin{aligned}S^2_{\rm VTI}(\theta) &= \frac{S_V{}^2\cos^2\theta+S_H{}^2\sin^2\theta+\sqrt{\left(S_V{}^2\cos^2\theta+S_H{}^2\sin^2\theta\right)^4+S_V{}^2\left(S_N{}^2-S_H{}^2\right)\sin^2 2\theta}}{2} \\ &= \frac{S^2_{\rm Ell}(\theta)+\sqrt{S^4_{\rm Ell}(\theta)+S_V{}^2\left(S_N{}^2-S_H{}^2\right)\sin^2 2\theta}}{2}, \qquad (58)\end{aligned}$$

where

$$S^2_{\rm Ell}(\theta) = {S_V}^2 \cos^2\theta + {S_H}^2 \sin^2\theta \tag{59}$$

is the elliptical component.

The derivatives are then written as:

$$\left.\frac{\partial S_{\rm VTI}(\theta)}{\partial \rho_{V_V}}\right|_{\rho=\mathbf{1}} = \frac{S_{\rm Ell}(\theta)}{2S_{\rm VTI}(\theta)}\frac{\partial S_{\rm Ell}(\theta)}{\partial \rho_{V_V}} + \frac{2\frac{\partial S_{\rm Ell}(\theta)}{\partial \rho_{V_V}} S^3_{\rm Ell}(\theta) - {S_V}^2\left({S_N}^2 - {S_H}^2\right)\sin^2 2\theta}{4S_{\rm VTI}(\theta)\sqrt{S^2_{\rm Ell}(\theta) + {S_V}^2\left({S_N}^2 - {S_H}^2\right)\sin^2 2\theta}} \tag{60}$$

$$\left.\frac{\partial S_{\rm VTI}(\theta)}{\partial \rho_{V_H}}\right|_{\rho=\mathbf{1}} = \frac{S_{\rm Ell}(\theta)}{2S_{\rm VTI}(\theta)}\frac{\partial S_{\rm Ell}(\theta)}{\partial \rho_{V_H}} + \frac{2\frac{\partial S_{\rm Ell}(\theta)}{\partial \rho_{V_H}} S^3_{\rm Ell}(\theta) + {S_V}^2{S_H}^2\sin^2 2\theta}{4S_{\rm VTI}(\theta)\sqrt{S^2_{\rm Ell}(\theta) + {S_V}^2\left({S_N}^2 - {S_H}^2\right)\sin^2 2\theta}} \tag{61}$$

$$\left.\frac{\partial S_{\rm VTI}(\theta)}{\partial \rho_{V_N}}\right|_{\rho=\mathbf{1}} = \frac{-{S_V}^2{S_N}^2\sin^2 2\theta}{4S_{\rm VTI}(\theta)\sqrt{S^2_{\rm Ell}(\theta) + {S_V}^2\left({S_N}^2 - {S_H}^2\right)\sin^2 2\theta}}, \tag{62}$$

where the derivatives of the elliptical component with respect to $\rho_{V_V}$ and $\rho_{V_H}$ are:

$$\left.\frac{\partial S_{\rm Ell}(\theta)}{\partial \rho_{V_V}}\right|_{\rho=\mathbf{1}} = \frac{-{S_V}^2\cos^2\theta}{S_{\rm Ell}(\theta)} \tag{63}$$

$$\left.\frac{\partial S_{\rm Ell}(\theta)}{\partial \rho_{V_H}}\right|_{\rho=\mathbf{1}} = \frac{-{S_H}^2\sin^2\theta}{S_{\rm Ell}(\theta)}. \tag{64}$$